Decomposition of silicon carbide at high pressures and temperatures

Kierstin Daviau and Kanani K. M. Lee

Phys. Rev. B **96**, 174102 — Published 3 November 2017

DOI: 10.1103/PhysRevB.96.174102

Decomposition of Silicon Carbide at High Pressures and Temperatures

Kierstin Daviau[1,*] and Kanani K. M. Lee[1]
[1]Department of Geology & Geophysics, Yale University, New Haven, CT 06511
[*]corresponding author; kierstin.daviau@yale.edu

ABSTRACT

We measure the onset of decomposition of silicon carbide SiC to silicon and carbon (e.g., diamond) at high pressures and high temperatures in a laser-heated diamond-anvil cell. We identify decomposition through x-ray diffraction and multi-wavelength imaging radiometry coupled with electron microscopy analyses on quenched samples. We find that B3 SiC (also known as 3C or zinc-blende SiC) decomposes at high pressures and high temperatures, following a phase boundary with a negative slope. The high-pressure decomposition temperatures measured are considerably lower than that at ambient, with our measurements indicating that SiC begins to decompose at ~2000 K at 60 GPa as compared to ~2800 K at ambient pressure. Once B3 SiC transitions to the high-pressure B1 (rocksalt) structure, we no longer observe decomposition, despite heating to temperatures in excess of ~3200 K. The temperature of decomposition and the nature of the decomposition phase boundary appear to be strongly influenced by the pressure-induced phase transitions to higher density structures in SiC, silicon and carbon. The decomposition of SiC at high-pressure and temperature has implications for the stability of naturally forming moissanite on Earth and in carbon-rich exoplanets.

I. INTRODUCTION

Silicon carbide (SiC) attracts a wide interest owing to its semiconductor nature, high bulk modulus and high melting temperature [1]. Naturally occurring SiC forms under very reducing conditions and is rare on Earth, found in small quantities in numerous geologic settings [2]. SiC is also abundant in the spectrum of carbon stars [3] and is found to be present in meteorites [4]. The discovery of extra-solar planets [5] and the possibility of carbon-rich solar systems largely composed of SiC [6,7] has expanded the areas in which we expect to find naturally occurring SiC, increasing the need for high-pressure and -temperature studies.

A large body of work has been performed to better understand aspects of the SiC phase diagram at various pressure and temperature conditions [8-21]. The ambient pressure, high temperature behavior of the Si-C system has been explored in detail [11]. Ambient temperature

studies have explored a wide range of pressure conditions. Zhuravlev et al., 2013 [20] proposed the use of SiC as a pressure standard in the diamond-anvil cell (DAC) based on elasticity studies carried out up to 80 GPa. It was found that cubic B3 SiC transforms to the B1 structure at a pressure of ~100 GPa when compressed in a DAC [19]. This transition was additionally observed in shock studies [13,15] and was recently reported at lower pressures of ~60 GPa when heated in a laser-heated DAC [10]. Additional studies of the high pressure and temperature (high P-T) behavior of SiC include measurements of the thermal equation of state (EOS) up to pressures of 8.1 GPa and temperatures of 1100 K [18] as well as the thermal expansion of SiC up to pressures of 80 GPa and temperatures of 1900 K [21].

Upon investigating the simultaneous high P-T behavior of SiC [10], we also found that SiC decomposes to its elemental constituents, silicon and carbon. This study focuses on the decomposition at high pressures and simultaneous high temperatures. At ambient pressures, it has been seen that SiC melts incongruently with the Si fraction coming out as a liquid and the C fraction remaining as a solid [11]. The ambient pressure decomposition of SiC into solid C plus liquid Si begins at ~ 2840 K in experiments [11] while it is predicted to occur at higher temperatures of 3100 K in computations [22,23]. Previous explorations of high-pressure melting and possible decomposition have gone up to ~ 10 GPa while heating to temperatures as high as 3500 K [8,9,12,14,16,17]. Confusion has arisen as to whether or not decomposition continues upon increasing pressure as well as the nature of the slope (positive or negative) of the phase boundary of the reaction. For instance, one study finds that SiC melts incongruently (decomposition to C solid and Si liquid) along a positively sloped phase boundary [17]. Based on the increase in the solubility of C in liquid Si with increasing pressure, they predict that decomposition does not continue past about ~10 GPa, after which SiC melts congruently. In nearly the same pressure and temperature range, another group [16] reports contradictory results, finding that SiC does not decompose at pressure and that congruent melting follows a negative phase boundary.

Using the laser-heated DAC in conjunction with a variety of in situ and ex situ quenched analysis techniques, we explore the decomposition behavior of SiC at pressures up to ~80 GPa and temperatures up to ~3200 K. Using x-ray diffraction (XRD), multi-wavelength imaging radiometry [24], Raman spectroscopy, focused ion beam (FIB) cross-sections and electron microscopy we investigate SiC decomposition at pressures between ~10 and 80 GPa. We find

that B3 SiC decomposes at pressure following a negative phase boundary. However, we do not observe decomposition in SiC after it transitions to the B1 structure even upon heating to a maximum temperature of ~3200 K at 81 GPa.

II. METHODS

Our samples consist of a fine-grained powder of cubic B3 SiC from Alfa Aesar (β-SiC product #14165, lot #I21X047), confirmed by XRD. We often observed additional weak reflections from the 101 and 103 hkl lines of 6H SiC in our starting diffraction patterns. Based on the relative intensities, however, the abundance of the 6H SiC (α-SiC) phase is likely less than 3%. Scanning electron microscope (SEM) images confirmed that the starting grain size varied between ~0.1 and 1 μm. For laser heating experiments, the powder was compressed in an 80-120 μm hole drilled in the center of a pre-indented Re gasket using the stepped anvil technique [25]. Both 200 and 300 μm culet diamonds were used. Several different materials were used as a pressure medium and thermal insulation including, NaCl, KCl, KBr, Ar, Ne, SiO_2 and self-insulation (no medium). Care was taken to dry out the samples by placing the completed samples into an oven at ~350 K overnight. Samples heated evenly and steadily with all materials except NaCl, where sample temperatures tended to run away, suggesting a change in the absorption character of NaCl at high temperatures, although no obvious color change was observed [26]. KCl, KBr, Ne and self-insulation were ultimately preferred to ensure steady heating and minimize contamination or oxidation of the SiC sample.

Pressure was measured using the Raman shift of the diamond edge [27] or, when available, the room temperature equation of state (EOS) of Ne [28] with corrections provided by [20]. The Raman system used is a Horiba-Jobin Yvon HR-800 Raman Microscope equipped with a 50mW green laser (532 nm) with an 1800 lines/mm grating (Table SI). After heating sample pressures typically increased by 10 to 20% in the heated region, although the largest pressure change observed was an increase by 50%. A couple of high-pressure samples dropped in pressure after heating (Table I and II). Our laser heating experiments were done in two locations: 1) at the HPCAT-IDB beamline at the Advanced Photon Source (APS) in which we used XRD to probe crystal structure and phase changes in situ [29] and 2) at Yale University where we used the multi-wavelength imaging radiometry temperature measurement system to map temperatures and emissivities to explore temperature gradients and corresponding optical

changes in SiC [24]. A combination of the findings from the two different kinds of experiments and ex situ analysis methods were used to constrain the onset of SiC decomposition at high P-T.

No matter the heating location, pressure medium, or starting pressure of the sample, the same procedure was followed in each heating experiment. Samples were heated systematically in the center of the sample chamber by gradually increasing laser power, remaining for several seconds to a minute at each power, and taking regularly-spaced temperature measurements to track the sample's response. For samples heated at HPCAT-IDB, diffraction patterns were also taken throughout the heating. After each heating round, the sample was temperature quenched and either a diffraction pattern (at HPCAT-IDB) or a white light image (at Yale University) was taken to characterize changes in the quenched sample as a result of the previous heating. Each sample was heated to a peak temperature between 1500 and 3200 K in this manner, aiming to increase the temperature by ~100 K increments. We ramp heated several samples [30] in order to account for diffusive effects brought about by the gradual temperature increase and long heating duration. We saw the same optical features and changes in both the gradually heated (over minutes) and ramp heated (over seconds) samples using the four-color temperature mapping technique.

Temperature was determined by measuring and fitting the thermal emission from the sample as described in [29] for those heated at HPCAT-IDB and in [24] for those heated at Yale. Wavelength-dependent absorption in laser-heated DAC samples has recently been identified as a potentially large source of error in spectroscopic temperature measurements [31]. In order to correct for this effect in our samples, we measured the absorption spectra of SiC at the offline VIS/IR lab at the National Synchrotron Light Source II (NSLS II) at Brookhaven National Lab (BNL). Absorption measurements over visible wavelengths were taken for both heated and unheated SiC at three different pressures (13, 35 and 52 GPa) in order to account for possible pressure effects in the absorption. Based on these measurements and the forward modeling outlined in [31], we find that our measured temperatures differ by only ~50 K from their predicted actual sample temperatures (Figure S2). Since the wavelength range used to calculate the temperature at the HPCAT-IDB heating system is a subset of the wavelength range used at Yale (~600-800 nm versus 580-905 nm), our temperature correction model can be applied to measurements taken at both locations. As our temperature error bars typically stretch to ±8% of the measured temperature [24], we do not additionally correct the measured temperatures for

absorption effects. Details of the absorption measurements and of the temperature correction forward modeling can also be found in the Supplemental Material.

Temperature quenched samples were further investigated by Raman spectroscopy at ambient and high pressures. Additionally, quenched samples were cross-sectioned using the FIB and analyzed by SEM for texture, energy dispersive spectroscopy (EDS) for qualitative composition, electron backscatter diffraction (EBSD) for crystal structure and electron probe microanalysis (EPMA) and wavelength dispersive spectroscopy (WDS) to determine quantitative composition. Further details of the analysis equipment can be found in Table SI of the Supplemental Material.

III. RESULTS

The two kinds of experiments allowed us to probe different in-situ properties during heating. Measurements done at the synchrotron determined structural changes through the use of XRD, while the measurements performed on the multi-wavelength imaging radiometry system determined optical changes and apparent temperature gradients across the hot sample through two dimensional temperature mapping. We first present the structural results from diffraction, and then present the optical results.

A. X-ray Diffraction

While heating SiC, we observe the emergence of new diffraction peaks corresponding to cubic diamond (Fig. 1a). The temperature and pressure of the diamond appearance, as well as the d-spacing of the diamond peaks from quenched patterns as compared to the calculated d-spacing, are listed in Table I. We take the formation of diamond in our SiC samples to indicate the onset of decomposition. Once formed, the diamond reflections remain even while heating to temperatures below the initial decomposition temperature. The diamond peaks also remain upon quench and decompression, indicating that the decomposition is irreversible on the timescales of our experiments. Due to our inability to reverse the experiments we are limited to only measuring the first onset of decomposition. Temperature gradients across the sample prevent us from determining the extent of decomposition as well. Due to the amount of cold material

through which the x-rays pass, the B3 SiC reflections never disappear and remain in samples even after decomposition has begun (see Supplemental Material).

We do not see the appearance of Si diffraction in any of our heating runs. There are several possibilities as to why this may be the case. At the high temperatures of SiC decomposition, Si is likely a liquid. The melting temperature of Si was experimentally measured to be low, around 1000 K, while at pressures up to ~15 GPa [32-34]. If the Si melting point remains low at increased pressures then we would not expect to see Si diffraction at high temperatures. Upon quenching the laser at high-pressure, Si may cool to an amorphous state [35], and therefore diffraction would not be observed. Impurities also play an important role in the structure of Si upon pressure unloading. It has been observed that Si quenches to an amorphous structure when unloaded in the presence of impurities [36]. If C is acting as the impurity in our system, it may prevent Si from crystallizing under pressure. This would result in Si being absent from both temperature-quenched and pressure-quenched XRD patterns.

The findings from the XRD measurements are supported by FIB-ed cross-sections of heated samples. Samples were cross-sectioned by first removing the excess gasket material with electrical discharge machining (EDM) and then FIB-ed using a FEI Helios Nanolab dual-beam system with Gallium ions (Ga^{+}) to etch away the unheated sample and reach the heated region [30]. We do not observe any adverse effects on the sample cross-section from the FIB process, as we polish the cross section with a very low ion current before doing any SEM or compositional analysis. We also check for any lingering Ga contamination in the sample and consistently find that the polished region of interest is free of Ga. Ga can collect in voids or cracks along the sample surface but remains localized and visible [37]. Once the hot spot was exposed and polished, we imaged the area with electron microscopy (XL-30 environmental SEM) and determined composition using EDS or WDS and EBSD analysis techniques. Figure 2 displays the map view of 4CLR_003, a sample heated at 39 GPa, as well as the back scattering electron (BSE) image of the cross section and the C and Si abundance WDS maps collected by EPMA. The dark grains in the BSE image correspond to regions of C enrichment and Si depletion, while the center of the heated area is slightly depleted in C and enriched in Si. We do not see any large, isolated grains of Si, consistent with Si forming small amorphous grains that remain invisible to x-rays. As we heat in one location throughout the experiment with a laser

spot size of ~20-30 μm, we only expect to see evidence of decomposition across a similarly sized region.

EBSD measurements were completed on a large carbon grain of ~ 4 μm found in cross section, confirming that the structure of the grain is cubic diamond (see Supplemental Material, Figure S5). We see considerable grain growth across the heated portion of this sample, and find that decomposition features are present across ~40 μm of the sample. Small diamond grains are found both on the interior and exterior of the SiC grains that began decomposition. The presence of Si, C and SiC grains after decomposition may contribute to the pressure increase observed after heating.

B. Multi-wavelength Imaging Radiometry

Using the multi-wavelength imaging radiometric temperature mapping system at Yale University we investigate the optical changes that SiC undergoes at high P-T [24]. The most dramatic change that we observe is a change in the sample's absorbance with increasing temperature. This absorbance change can be seen clearly in both the emissivity (light intensity from thermal emission) and the temperature measurements from our system. Changes in sample emissivity have been used previously as a diagnostic for phase changes [38,39] as emissivity is a material property.

Our starting powder is semi-opaque when loaded and remains so after compression, even at the highest pressures attained in these experiments. Transmitted light measurements on our laser heating system record only a very dim passage of white light through the starting material. After heating to low temperatures (~1000 K) the SiC begins to lose its opacity and becomes more transparent to white light. The transmitted light images collected by CCD show a transparent disk covering the area of the sample that has been heated. At higher temperatures samples develop dark, absorbing spots in the heating location. These appear as absorbing features in the middle of the transparent disk (Fig. 1b, Fig. 3e).

We can see evidence of these absorbing features in the temperature and emissivity maps collected during heating (Fig. 3). At low temperatures, below decomposition of SiC, the temperature and emissivity maps show similar symmetric profiles: highest values at the center with decreasing values radially outward. Samples heated to high enough temperatures to become

absorbing continue to show symmetric emissivity maps, however temperature maps no longer record highest apparent temperatures at their centers, suggesting wavelength-dependency of the absorption (Fig. 3f-g). The apparent temperature maps instead indicate that the center is *cooler* than the edges and have a reverse profile with increasing temperature around the *edge* of the heating area. We report the temperature surrounding the apparent cooler region. In order to explain the apparent temperature decrease, we forward model the temperatures [31] using the measured absorption profiles and estimates of the cross-sectional layer thicknesses. This mismatch between the temperature and emissivity maps is due to the highly absorbing and wavelength-dependent characteristics of the heated area. The dark feature blocks out a portion of the thermal emission in a wavelength-dependent fashion, meaning that even though the center of the laser spot gives the most counts, it does not fit a blackbody corresponding to the highest temperature. The difference appears to be small, however, with temperature aliasing typically less than 100 K across the heated area (~20 μm). See the Supplemental Material for a detailed discussion of the temperature correction forward model.

Table II lists the pressure and temperature conditions at which samples first displayed characteristics of the highly absorbing feature. The feature was identified by the mismatch between the emissivity and temperature maps and confirmed by post-heat white light images when available (Fig. 3). Our interpretation of these features is further informed by the appearance of carbide-derived carbon (CDC) signals in the Raman spectra [40] (Fig. 4, see Supplementary Material) as well as the features observed in FIB-ed cross-sections. The initial shift to optical transparency may be due to the annealing of dislocations and reorganization of grain boundaries, as the transparency of SiC has previously been correlated with grain orientation and internal microstructure [41]. We do not consistently see structural changes in SiC at low temperatures in the XRD, and the lower temperature regions of cross sections are featureless aside from considerable grain growth as compared to the starting material.

The sudden increase in absorption appears to be related to decomposition based on the strong correlation between the P-T conditions at which we see diamond XRD peaks emerge and the conditions at which the strongly absorbing features appear. We use the change in the temperature maps as evidence for the absorbing feature and, therefore, SiC decomposition. Similar to the diamond XRD peaks, once the heated SiC forms an opaque region at high temperature it does not revert back to more transparent at lower temperatures or upon

decompression. As both the phases of carbon (graphite and diamond depending on pressure [42]) and the phases of silicon (I, II, V depending on pressure [43,44]) have very different optical properties from one another and from SiC, it is not surprising that the break down of SiC to C and Si will result in visible changes across the heated area. It is possible that the absorbing feature is due to the presence of elemental Si forming upon decomposition.

IV. DISCUSSION

We make several unexpected observations in our decomposition measurements. The first observation is that the onset of decomposition at 10 GPa occurs at ~2300 ± 200 K. The closest study finding decomposition of SiC in previous work is at 3400 K at 9 GPa [17]. If both the previous data point and our data point are reliable, then this requires a steep drop in the decomposition temperature of over 1000 K across a pressure range of only one GPa. At pressures above 10 GPa we do see a drop in the decomposition temperature with increasing pressure but following a much shallower transition boundary. In the previous study, the temperatures reported are calculated by correcting the amount of inserted energy for heat loss and then converting to temperature using the temperature dependence of the enthalpy of SiC from the National Institute of Standards and Technology Joint Army Navy and Air Force (*NIST-JANAF*) thermochemical tables [45]. It is also possible that their measurements may not be for the onset of decomposition, but rather well in to decomposition [17].

We find a second unexpected aspect of SiC decomposition at higher pressure. At 81 GPa, SiC did not heat smoothly as observed at lower pressures. The sample instead showed only a slight glow when heating, indicating that temperatures were low, however, the sample quickly became more absorbing and the temperatures rapidly rose, but did not runaway. We see no evidence of decomposition in the Raman spectra across the hottest region of that sample, which was heated to over 3200 K (Fig. 4). However, in the surrounding SiC that was annealed to very low temperatures (~1200 K) without any sudden coupling we see the D and G band signatures of CDC in the Raman spectra taken after decompression (Fig. 4).

We explain these two unexpected features by considering the phase changes of SiC, Si and C at high pressures. If we consider the phase diagrams and room temperature equations of state for all three materials, we see that our unexpected observations fall at pressure conditions

near where a phase change has been observed in at least one of the three components in the system. In Figure 5 we plot the compression curves for SiC, Si and C, as well as the corresponding volume changes across the $SiC \rightarrow Si + C$ decomposition reaction. Positive values of ΔV mean that $Si + C$ has a larger volume per (Si, C) atom pair than SiC, while negative values of ΔV mean that SiC has the larger volume. At low pressures, when Si and C are both in their lowest pressure structures, the volume change across the decomposition reaction is large and positive. This is consistent with low pressure measurements finding a high decomposition temperature and positive Clapeyron slope [17]. At slightly higher pressures, however, both C and Si transition to higher density structures, with the largest compaction occurring in the Si structure going from the diamond (Si-I) to β-Sn (Si-II) structure (~12 GPa at room temperature) [44]. Because of this sudden increase in Si density, the volume change across the decomposition of SiC drops to negative values. While SiC remains in its low-pressure B3 structure but Si transitions to several high-pressure, higher-density structures, the volume change across the decomposition reaction remains negative and increases in magnitude. The abrupt change in ΔV at the transition from Si-I to Si-II may explain why we see such a large drop in decomposition temperature at pressures of ~10 GPa as compared to ambient and lower pressure measurements. The negative ΔV at higher pressures is consistent with the negative slope of the phase boundary that we observe for the reaction up to ~62 GPa.

Above 60 GPa, SiC transitions from the B3 to the B1 structure at equilibrium. This transition is known to be sluggish [10], however, and is not observed until ~100 GPa at room temperature [19]. Recent work finds that the addition of temperatures near 1700 K lowers the transition pressure closer to that expected from computations [10]. The B3 to B1 transition is accompanied by a nearly 20% decrease in volume, which is enough to switch the sign of ΔV across the decomposition reaction back to positive values. Our measurements at 81 GPa can be explained if they are straddling the B3 to B1 transition in SiC. At these pressures and temperatures the hottest region of the sample is likely in the B1 structure [10]. We see an additional peak at ~1470 cm^{-1} in the Raman spectra of the hottest region that is not found in the surrounding annealed SiC or upon quench (Fig. 4). In the B1 structure it appears to take very high temperatures to achieve decomposition, at least over 3200 K at ~80 GPa if decomposition occurs at all. B1 SiC may decompose at higher temperatures than those explored here, perhaps following a positive Clapeyron slope as indicated by the volume change across the

decomposition reaction. Based on the differences in volume, at pressures greater than ~170 GPa, decomposition may require lower temperatures and follow a negative phase boundary once again (Fig. 5). The surrounding portion of the sample that was annealed at low temperatures (<~1200 K) did not reach a high enough temperature to transition to the B1 structure but did reach high enough temperatures to decompose the metastable B3 SiC. Decomposition in metastable B3 SiC would still have a large negative ΔV across the transition and so, based on our data at lower pressures, would decompose at a low annealing temperature.

We present a phase diagram for the decomposition of SiC at high pressures and temperatures based on our experimental work as well as that reported by previous studies (Fig. 6) [11,16,17]. The shape of the decomposition boundary appears to be strongly influenced by the structural transitions in the Si, C and SiC components. As we did not measure decomposition in the B1 structure, we do not include a decomposition boundary for B1 SiC, although it may decompose at higher temperatures than those explored here. At the temperatures of decomposition Si is likely a liquid [32-34], and thus the decomposition of B3 SiC is an example of incongruent melting. It is possible that B1 SiC is stable to high enough temperatures to melt congruently and so does not undergo decomposition. We note that below 60 GPa, high temperature B3 SiC does not favor a transition to B1 SiC over decomposition due to a Clapeyron slope near zero for the B3 to B1 transition at equilibrium conditions [10].

In this way we are able to join our high-pressure results with those conducted at lower pressures [16,17], resolving some of the confusion and inconsistencies with the previous studies. We are still unsure, however, why [16] observed melting of SiC but not decomposition at pressures of 5 and 7.5 GPa. It is possible that the SiC in their experiments was still below the decomposition temperature since we expect the Clapeyron slope to be positive in this pressure regime, although we would not expect to see any melting if this is the case. What is interesting about this region is that it is above the transition pressure of C graphite to C diamond but below the transition of Si I to Si II. It is possible that the decomposition reaction behaves differently in this window where diamond is stable but the ΔV across the transition is still positive. As an alternative explanation for the lack of observations of diamond formation in [16], we suggest that the small grain size may have made diamond difficult to detect in quenched diffraction analyses. We find that our diamond grains are very small, on the order of several μm at most, and quite localized. Moving even 5 μm away from the heating location causes the diamond diffraction to

disappear in most of our experiments. It would be difficult to locate a diamond grain in a post-heated sample that had been formed away from a synchrotron x-ray diffraction beam line, making it challenging to determine with certainty that a sample did not decompose.

Kinetic effects may also contribute to differences between the previous and current studies. The B3 to B1 transition in SiC is kinetically hindered [10] as is transitions in other carbon materials (e.g., [46,47]). We find here that decomposition of SiC is also kinetically slow, meaning that grain size may play a role in the extent of decomposition observed. Our starting grain size ranges from 0.1 to 1 μm, while [16] used single crystals ranging from 150 μm to 3 mm in size. The slow kinetics of decomposition may have prevented [16] from easily observing the transition in the large single crystals.

Another potential source of offset between the transition conditions observed in our study from the previous studies is the methods used for temperature measurement. We directly measure temperature using the thermal emission of the sample, while the previous studies indirectly calculated temperature from the amount of inserted energy by the power source [17] or through known standard calibrations [16,48]. This difference may account for some of the discrepancy between the lower pressure decomposition temperatures in the previous studies and the higher-pressure decomposition temperatures measured here. However, the data as it currently stands can still be explained by the change in the sign of the ΔV across the decomposition boundary from positive to negative at ~12 GPa, as is shown in Figure 5.

The decomposition of SiC at pressure has implications for several fields. Natural SiC (moissanite after its discovery in the Canyon Diablo meteorite by Henri Moissan [49]) is rare on Earth, but nevertheless has been found in small quantities in numerous geologic settings [2,50]. A common assumption is that SiC is stable at all pressure and temperature conditions found within the Earth's lower mantle if the local chemistry favors SiC formation [51,52]. Our findings, however, indicate that SiC has a layer of instability within the Earth's mantle stretching from ~50 GPa to 60 GPa along a typical Earth geotherm [53] or from ~40 GPa to 60 GPa along a warmer geotherm [54]. This corresponds to a layer stretching from between ~1250 to ~1500 km deep along the typical geotherm or from ~1000 to 1500 km deep along the warmer geotherm where any existing SiC would decompose to Si + C. Our work indicates that the SiC forming on Earth must originate from shallower depths, as it would not be preserved on a journey up through this layer from the deep mantle. An exception is within subducting slabs, where the temperature

conditions would remain low enough to keep B3 SiC stable at pressures below the B3 to B1 transition [55]. Interestingly, many natural SiC grains contain Si inclusions [56]. We offer a possible additional interpretation of such Si inclusions as being relics from previous SiC decomposition.

Beyond the Earth, the decomposition of SiC is also important to consider for exoplanet interiors, particularly in carbon-rich solar systems. Planets with interior temperatures of over 2000 K at pressures less than 60 GPa will decompose to B3 SiC. If SiC makes up a significant fraction of a planet then the presence of C and Si rather than SiC may impact the dynamics and interior structure of such a planet.

Decomposition at high temperature is a phenomenon found in many semiconductors besides SiC although pressure effects on their decomposition are not yet well understood (i.e., [57-60]). If we consider the ΔV of decomposition for other semiconductors we find that those containing elements heavier than carbon (such as nitrogen) are much less likely to enter a regime where the volume change across the decomposition reaction is negative, due to the larger volume of the components [61]. This may mean that the Clapeyron slope for decomposition remains positive for nitrogen-bearing semiconductors unlike the negative slope that we observe for SiC. Further investigation is necessary at high P-T conditions however, to further our understanding of decomposition in semiconductors.

V. CONCLUSIONS

Through a combination of in situ and ex situ measurements, we determine the temperature of the onset of decomposition in SiC at high pressures. We find that low pressure B3 SiC decomposes at temperatures ~ 500 K lower compared to ambient, possibly due to the transition of Si I to the high-density Si-II structure. We find that B1 SiC does not decompose at the temperatures considered (up to ~3200 K at 81 GPa). We present the first phase diagram for SiC decomposition at high P-T and reconcile the conflicting findings of previous studies. From our measurements we infer that the shape of the phase boundary is heavily influenced by the numerous phases of carbon and silicon and their respective phase diagrams and equations of state, in addition to the high-pressure phase transition from the B3 to the B1 structure in SiC. We find that if SiC decomposition continues to occur beyond the B3→B1 phase transition, it will

require temperatures in excess of 3200 K at ~80 GPa; but at pressures greater than ~170 GPa, decomposition may occur at lower temperatures again following a negative phase boundary.

ACKNOWLEDGEMENTS

We acknowledge support from the Carnegie DOE Alliance Center (CDAC). We thank J. Deng for helpful discussions, J. Girard for technical assistance, Z. Jiang and J. Eckert for SEM and EPMA assistance, and Z. Liu for assistance in VIS/IR measurements. We also thank Yue Meng and Ross Hrubiak for assistance at the HPCAT IDB beamline as well as Sergey Tkachev for gas loading with the system at GSECARS. This work was performed at HPCAT (Sector 16), APS, Argonne National Laboratory. HPCAT operations are supported by DOE-NNSA under Award No. DE-NA0001974 and DOE-BES under Award No. DE-FG02- 99ER45775, with partial instrumentation funding by NSF. Use of the COMPRES-GSECARS gas loading system was supported by COMPRES under NSF Cooperative Agreement EAR 11–57758 and by GSECARS through NSF Grant No. EAR-1128799 and DOE Grant No. DE-FG02-94ER14466. This research used resources of the APS, a U.S. Department of Energy (DOE) Office of Science User Facility operated for the DOE Office of Science by Argonne National Laboratory under Contract No. DE-AC02-06CH11357. This research used resources of the Center for Functional Nanomaterials, which is a U.S. DOE Office of Science Facility, at Brookhaven National Laboratory under Contract No. DE-SC0012704. The Infrared Laboratory is supported by COMPRES, under NSF Cooperative Agreement EAR 1606856 and the DOE/National Nuclear Security Administration under Grant DE-NA-0002006, CDAC. The National Synchrotron Light Source II is supported by the DOE Office of Science under Contract No. DE-SC0012704.

References

[1] G. L. Harris, *Properties of silicon carbide* (Iet, 1995), 13.
[2] V. Lyakhovich, International Geology Review **22**, 961 (1980).
[3] A. Speck, M. Barlow, and C. Skinner, Monthly Notices of the Royal Astronomical Society **288**, 431 (1997).
[4] S. Amari, R. S. Lewis, and E. Anders, Geochimica et Cosmochimica Acta **58**, 459 (1994).
[5] M. Mayor and D. Queloz, Nature **378**, 355 (1995).
[6] M. J. Kuchner and S. Seager, arXiv preprint astro-ph/0504214 (2005).
[7] N. Madhusudhan, K. K. M. Lee, and O. Mousis, The Astrophysical Journal Letters **759**, L40 (2012).
[8] S. Bhaumik, Metals Materials And Processes **12**, 215 (2000).
[9] S. Bhaumik, C. Divakar, M. Mohan, and A. Singh, Review of scientific instruments **67**, 3679 (1996).
[10] K. Daviau and K. K. M. Lee, Physical Review B **95**, 134108 (2017).

[11] R. Dolloff and R. Sara, *Research study to determine the phase equilibrium relations of selected metal carbides at high temperatures* (Wright Air Development Division, Air Research and Development Command, United States Air Force, 1960).
[12] E. Ekimov, R. Sadykov, S. Gierlotka, A. Presz, E. Tatyanin, V. Slesarev, and N. Kuzin, Instruments and Experimental Techniques **47**, 276 (2004).
[13] W. Gust, A. Holt, and E. Royce, Journal of Applied Physics **44**, 550 (1973).
[14] H. T. Hall, Final report US Army Office of Ordnance Research, contract No. DA 04 495 ORD 792, Brigham Young University, 36 (1956).
[15] T. Sekine and T. Kobayashi, Physical Review B **55**, 8034 (1997).
[16] P. S. Sokolov, V. A. Mukhanov, T. Chauveau, and V. L. Solozhenko, Journal of Superhard Materials **34**, 339 (2012).
[17] M. Togaya and S. Sugiyama, 高圧力の科学と技術= The Review of high pressure science and technology **7**, 1037 (1998).
[18] Y. Wang, Z. T. Liu, S. V. Khare, S. A. Collins, J. Zhang, L. Wang, and Y. Zhao, Applied Physics Letters **108**, 061906 (2016).
[19] M. Yoshida, A. Onodera, M. Ueno, K. Takemura, and O. Shimomura, Physical Review B **48**, 10587 (1993).
[20] K. K. Zhuravlev, A. F. Goncharov, S. N. Tkachev, P. Dera, and V. B. Prakapenka, Journal of Applied Physics **113**, 113503 (2013).
[21] C. Nisr, Y. Meng, A. MacDowell, J. Yan, V. Prakapenka, and S. H. Shim, Journal of Geophysical Research: Planets **122**, 124 (2017).
[22] J. Gröbner, H. L. Lukas, and F. Aldinger, Calphad **20**, 247 (1996).
[23] P. Franke, D. Neuschütz, and S. G. T. Europe, (Springer Materials, 2004).
[24] Z. Du, G. Amulele, L. Robin Benedetti, and K. K. M. Lee, Review of Scientific Instruments **84**, 075111 (2013).
[25] Z. Du, T. Gu, V. Dobrosavljevic, S. T. Weir, S. Falabella, and K. K. M. Lee, Review of Scientific Instruments **86**, 095103 (2015).
[26] S. Arveson, B. Kiefer, Z. Liu, and K. K. M. Lee, (2017 (Under Review)).
[27] Y. Akahama and H. Kawamura, Journal of applied physics **96**, 3748 (2004).
[28] Y. Fei, A. Ricolleau, M. Frank, K. Mibe, G. Shen, and V. Prakapenka, Proceedings of the National Academy of Sciences **104**, 9182 (2007).
[29] Y. Meng, G. Shen, and H. Mao, Journal of Physics: Condensed Matter **18**, S1097 (2006).
[30] Z. Du and K. K. Lee, Geophysical Research Letters **41**, 8061 (2014).
[31] J. Deng, Z. Du, L. R. Benedetti, and K. K. M. Lee, Journal of Applied Physics **121**, 025901 (2017).
[32] A. Kubo, Y. Wang, C. E. Runge, T. Uchida, B. Kiefer, N. Nishiyama, and T. S. Duffy, Journal of Physics and Chemistry of Solids **69**, 2255 (2008).
[33] F. Bundy, The Journal of Chemical Physics **41**, 3809 (1964).
[34] A. Jayaraman, W. Klement Jr, and G. Kennedy, Physical Review **130**, 540 (1963).
[35] S. K. Deb, M. W. M. Somayazulu, and P. F. McMillan, Nature **414**, 528 (2001).
[36] B. Haberl, M. Guthrie, D. Sprouster, J. Williams, and J. Bradby, Journal of Applied Crystallography **46**, 758 (2013).
[37] T. Gu, M. Li, C. McCammon, and K. K. Lee, Nature Geoscience **9**, 723 (2016).
[38] A. J. Campbell, Review of Scientific Instruments **79**, 015108 (2008).
[39] R. A. Fischer and A. J. Campbell, American Mineralogist **95**, 1473 (2010).

[40] Z. Cambaz, G. Yushin, Y. Gogotsi, K. Vyshnyakova, and L. Pereselentseva, Journal of the American Ceramic Society **89**, 509 (2006).
[41] Y. Kim, A. Zangvil, J. S. Goela, and R. L. Taylor, Journal of the American Ceramic Society **78**, 1571 (1995).
[42] F. Bundy, The Journal of Chemical Physics **38**, 631 (1963).
[43] S. J. Duclos, Y. K. Vohra, and A. L. Ruoff, Physical Review B **41**, 12021 (1990).
[44] J. Hu and I. Spain, Solid state communications **51**, 263 (1984).
[45] J. T. Tables, Washington, DC **20234** (1971).
[46] Y. Wang, J. E. Panzik, B. Kiefer, and K. K. Lee, Scientific reports **2** (2012).
[47] J. M. Montgomery, B. Kiefer, and K. K. Lee, Journal of Applied Physics **110**, 043725 (2011).
[48] V. A. Mukhanov, P. S. Sokolov, and V. L. Solozhenko, Journal of Superhard Materials **34**, 211 (2012).
[49] H. Moissan, Comptes rendus **139**, 773 (1904).
[50] R. B. Trumbull, J.-S. Yang, P. T. Robinson, S. Di Pierro, T. Vennemann, and M. Wiedenbeck, Lithos **113**, 612 (2009).
[51] G. C. Ulmer, D. E. Grandstaff, E. Woermann, M. Gˆbbels, M. Schˆnitz, and A. B. Woodland, Neues Jahrbuch f¸ r Mineralogie-Abhandlungen, 279 (1998).
[52] E. Mathez, R. Fogel, I. Hutcheon, and V. Marshintsev, Geochimica et Cosmochimica Acta **59**, 781 (1995).
[53] J. Brown and T. Shankland, Geophys J Int **66**, 579 (1981).
[54] O. L. Anderson, Evolution of the Earth, 19 (1981).
[55] E. Ohtani, Chemical Geology **418**, 6 (2015).
[56] L. Dobrzhinetskaya, P. Mukhin, Q. Wang, R. Wirth, E. O'Bannon, W. Zhao, L. Eppelbaum, and T. Sokhonchuk, Lithos (2017).
[57] S. Porowski, B. Sadovyi, S. Gierlotka, S. Rzoska, I. Grzegory, I. Petrusha, V. Turkevich, and D. Stratiichuk, Journal of Physics and Chemistry of Solids **85**, 138 (2015).
[58] H.-F. Lee, K. Esfarjani, Z. Dong, G. Xiong, A. A. Pelegri, and S. D. Tse, ACS nano **10**, 10563 (2016).
[59] L. H. Dreger, V. Dadape, and J. L. Margrave, The Journal of Physical Chemistry **66**, 1556 (1962).
[60] A. Edwards, T. Slykhouse, and H. Drickamer, Journal of Physics and Chemistry of Solids **11**, 140 (1959).
[61] M. Eremets, A. Gavriliuk, N. Serebryanaya, I. Trojan, D. Dzivenko, R. Boehler, H. Mao, and R. Hemley, The Journal of chemical physics **121**, 11296 (2004).
[62] W. Lee and X. Yao, Computational Materials Science **106**, 76 (2015).
[63] I. Aleksandrov, A. Goncharov, A. Zisman, and S. Stishov, Zh. eksp. teor. Fiz **93**, 691 (1987).

Figure Captions

FIG. 1 a) Diffraction patterns of temperature quenched samples from before, during double-sided laser heating and after heating B3 SiC at ~20 GPa (XRD_002). The hkl reflections of B3

SiC and Ne are labeled, as well as those from C diamond that appears after heating to high temperatures. In this case diamond appeared at upstream (downstream) temperatures of 2160 K (2333 K), but the temperature was increased to over 2400 K before taking a temperature-quenched pattern. Reflections from the Re gasket are labeled with an asterisk "*", reflections from 6H-SiC are labeled with a star "□", and an unidentified peak appearing at high temperature is labeled with the marker "o". **b)** Optical images of the same sample taken after heating. The top image is of the sample under pressures at ~22 GPa while the bottom image is after decompression. There are three different regions of the sample: 1) grey, unheated material on the outer edge of the sample chamber, 2) translucent material surrounding the hottest region and 3) a black, opaque center where the laser was focused and temperatures, presumably, the hottest. We do not observe evidence for diamond anvil damage upon unloading the sample.

FIG. 2 a) Photomicrograph of 4CLR_003, heated at 39 GPa, displaying characteristic optical changes across the heated location using both transmitted and reflected light. **b)** BSE image of the corresponding FIB-ed cross-section across the hot spot. Compositional map of sample cross sections measured by EPMA EDS of **c)** C and **d)** Si. Brighter areas denote higher relative abundance, while darker areas denote lower relative abundance. We observe concentrated C-rich and Si-poor grains as well as a larger central region with slight Si enrichments.

FIG. 3 Progression of the absorption changes observed in a 42 GPa sample laser heated with temperatures measured by multi-wavelength imaging radiometry [24]. The top row of images is of the sample in the 640 nm wavelength captured by the CCD camera during the heating experiment. The bottom row contains the corresponding emissivity and temperature maps found by fitting three additional wavelength images (580, 766, 905 nm). Top row from left to right: a) transmitted white light through the sample after initial annealing at low temperatures; b) in situ thermal emission from mid-way through heating (52 W of laser power); c) white light image after 52 W heating. Note enhanced transparency as compared to surrounding areas; d) in situ thermal emission of final heating at 68 W; e) white light after final 68 W heating. Bottom row from left to right: f) in situ emissivity and temperature map from the 52W heating; g) in situ emissivity and temperature map from the 68W heating. Notice that the sample becomes significantly more transparent over the heated region (green outline) and that a darker region becomes apparent in the white light image after the final heating. The emissivity and temperature maps match up well during the early heating but become uncorrelated later in the heating run. Green outlines correspond to the region of the image where temperature and emissivity are mapped.

FIG. 4 Raman spectra from 4CLR_006 after heating at 81 GPa using the four-color temperature mapping system. The top two patterns are of the compressed sample while the bottom two patterns are of the same sample after unloading from the diamond cell. We see a small additional peak at ~1470 cm^{-1} in the center of the heated area while at pressure that is absent

from the surrounding region as well as from the unloaded pattern. After unloading we see no evidence of decomposition throughout the hottest region but do see the characteristic D and G band signals of CDC in the surrounding, annealed area. The lack of decomposition in the hot spot is supported by in situ measurements, as throughout the entire heating and up to the highest temperatures of ~3200 K, the temperature and emissivity maps continue to display symmetric behavior across the hot spot.

FIG. 5 The room-temperature equations of state for SiC [20,62], Si [43] and C [42,63] including high-pressure phase transitions (solid curves) as well as the curve for $\Delta V = [(V_{Si} + V_C) - V_{SiC}]$ across the SiC to Si + C decomposition reaction (dashed curve). The ΔV for decomposition is large and positive at low pressures (<~12 GPa) but decreases to negative values upon the transition of Si I to Si II. The ΔV remains negative until B3 SiC transitions to the higher density B1 structure. At equilibrium, this reaction occurs at ~58 GPa (i.e, [62]) but is kinetically hindered experimentally and is not seen before 100 GPa at room temperature [19]. The shaded region of the SiC and ΔV curve represents the region across which the SiC volume, and therefore the ΔV at decomposition, is dependent on the experimental conditions.

FIG. 6 Phase diagram for the high-pressure decomposition of SiC. Conditions at which the first sign of diamond diffraction appears are represented by solid circles, conditions at which absorption changes are observed by multi-wavelength imaging radiometry are represented by solid triangles and the conditions at which B1 SiC shows no evidence of decomposition is represented by an open square. Temperature error bars are as described in Table I and Table II. Pressure error bars for the diffraction data are from errors in the Ne volume and are smaller than the symbols [20,28]. Pressure error bars for the four-color measurements are from the spread in pressure across the sample chamber before and after heating as determined by the Raman edge of diamond [27]. Previous data observing decomposition is represented by solid diamonds [11] and by asterisks for the previously reported extrapolated phase boundary [17]. Previous data that did not observe decomposition is represented by plus signs [16]. We show the regions of phase stability through colored shading with blue corresponding to B3 SiC, green to Si+C, pink to B1 SiC and the mixed purple region representing the area where the B3 to B1 transition is kinetically hindered. Temperature profiles for Earth's mantle [53,54] as well as for a subducting slab [55] are plotted. Both mantle geotherms cross the decomposition boundary for SiC, indicating that moissanite has a region of instability within the mantle.

FIG. 1

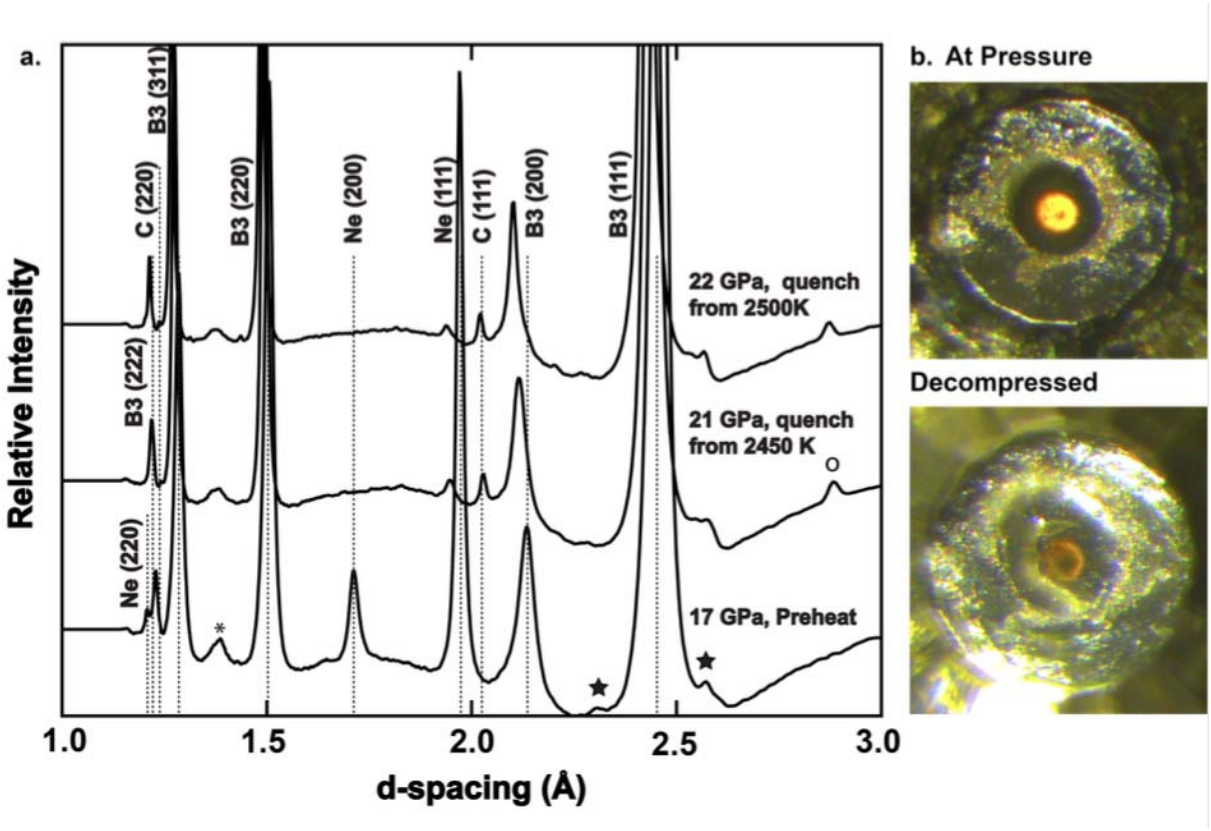
a.
b. At Pressure
Decompressed
Relative Intensity
d-spacing (Å)
1.0
1.5
2.0
2.5
3.0
Ne (220)
B3 (222)
C (220)
B3 (311)
B3 (220)
Ne (200)
Ne (111)
C (111)
B3 (200)
B3 (111)
22 GPa, quench from 2500K
21 GPa, quench from 2450 K
17 GPa, Preheat
*
o

FIG. 2

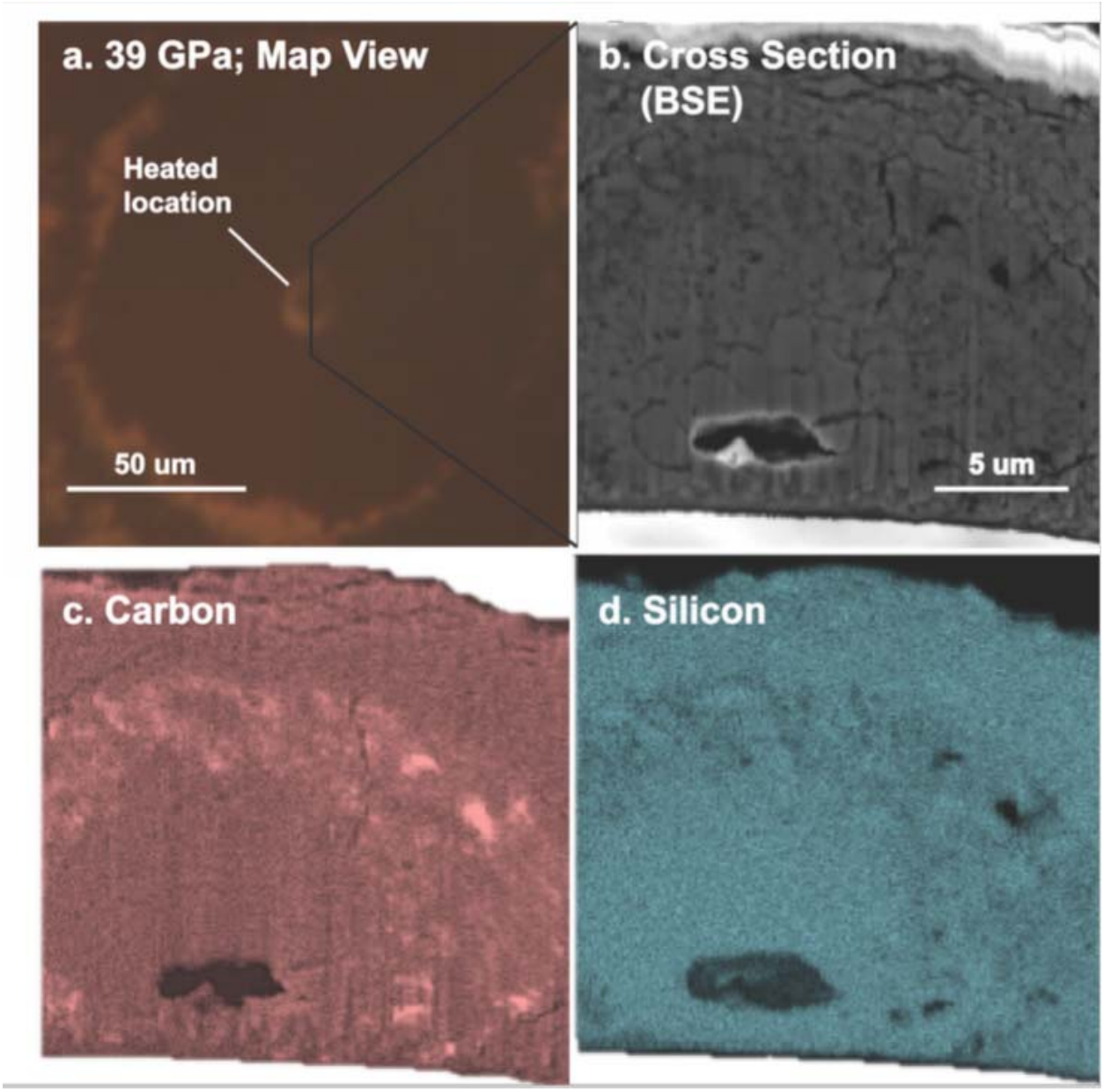
a. 39 GPa; Map View
Heated location
50 um
b. Cross Section (BSE)
5 um
c. Carbon
d. Silicon

FIG. 3

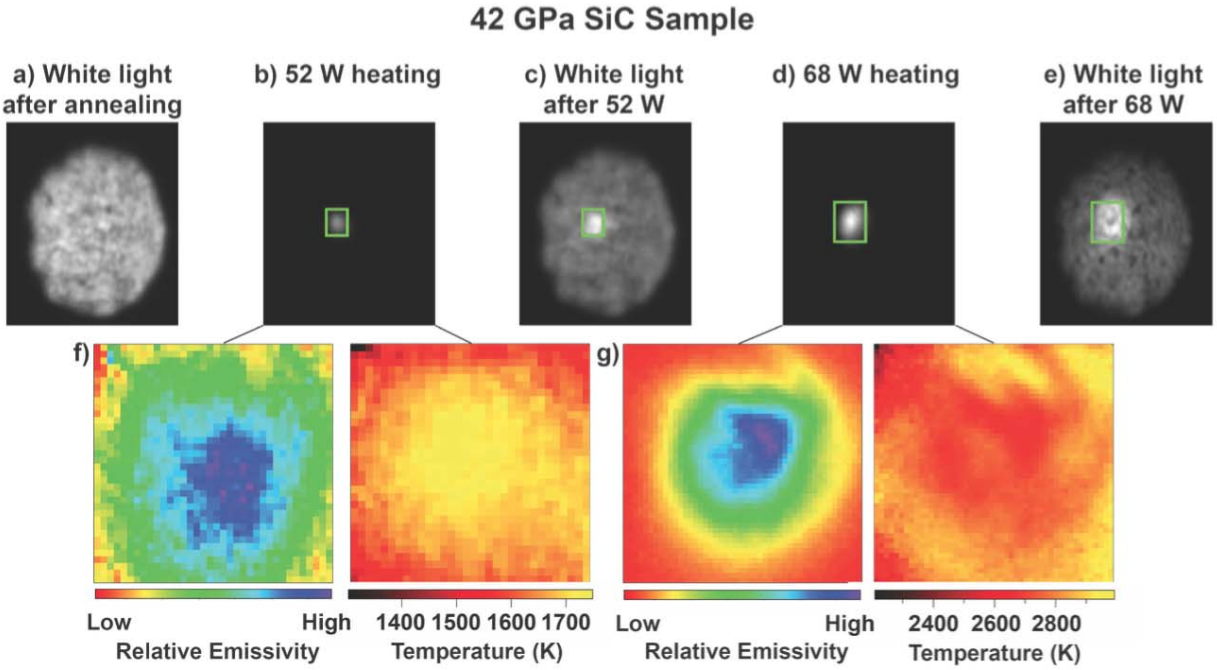
42 GPa SiC Sample
a) White light after annealing
b) 52 W heating
c) White light after 52 W
d) 68 W heating
e) White light after 68 W
f)
g)
Low
High
Relative Emissivity
1400 1500 1600 1700
Temperature (K)
Low
High
Relative Emissivity
2400 2600 2800
Temperature (K)

675 FIG. 4

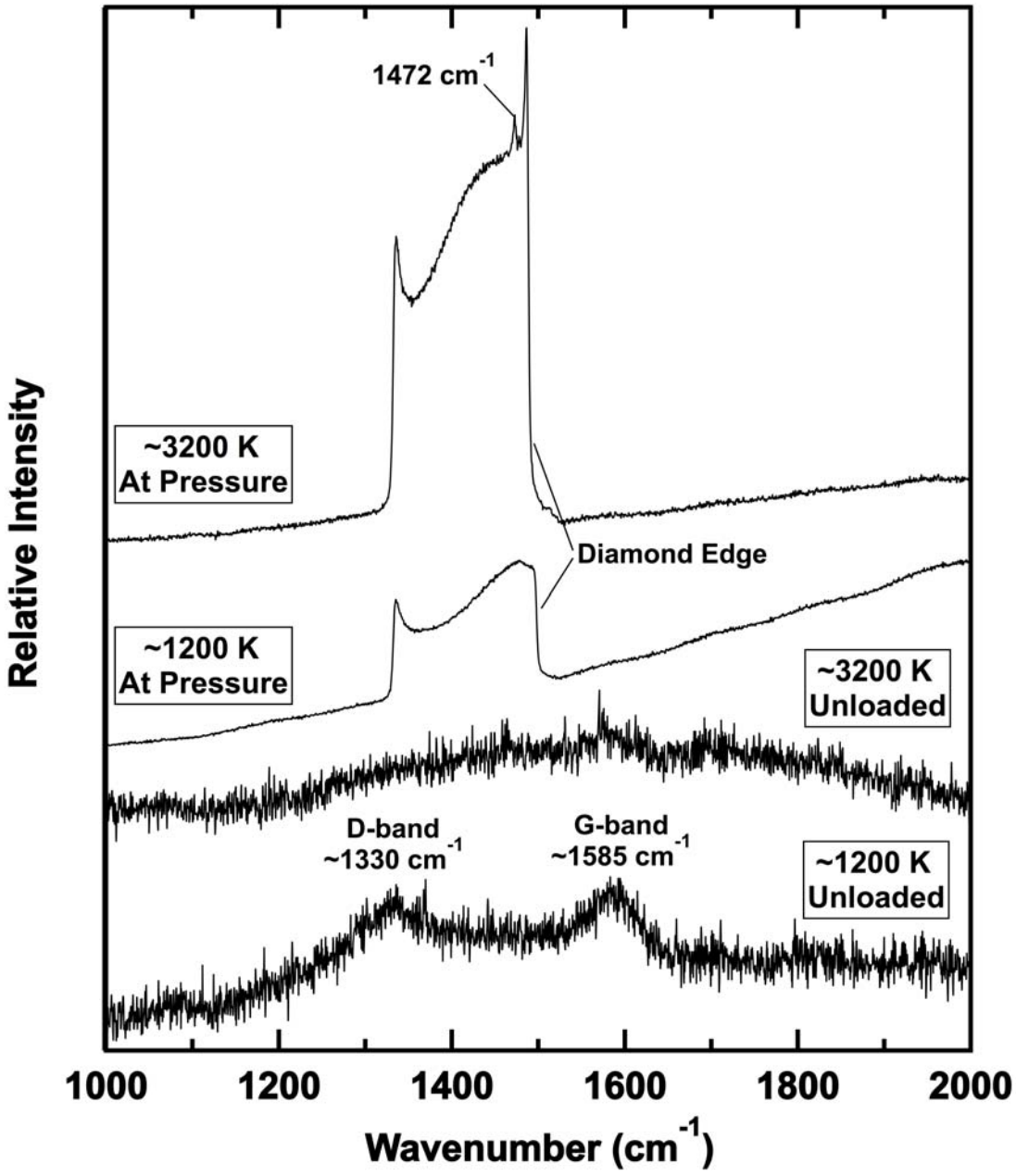

676
677
678
679
680
681
682
683
684

FIG. 5

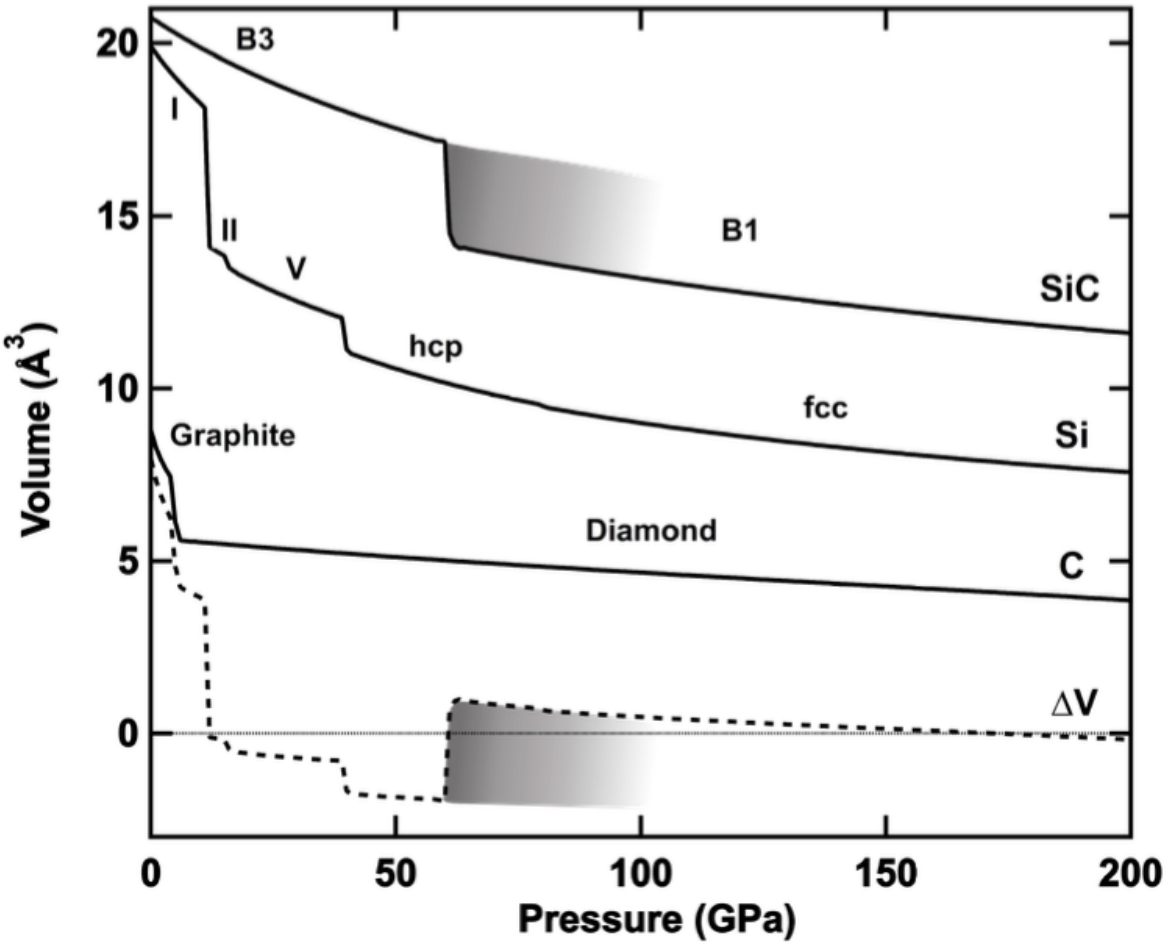
B3
I
II
V
B1
SiC
hcp
fcc
Si
Graphite
Diamond
C
ΔV
Volume (Å^3)
Pressure (GPa)
0
5
10
15
20
0
50
100
150
200

703 FIG. 6

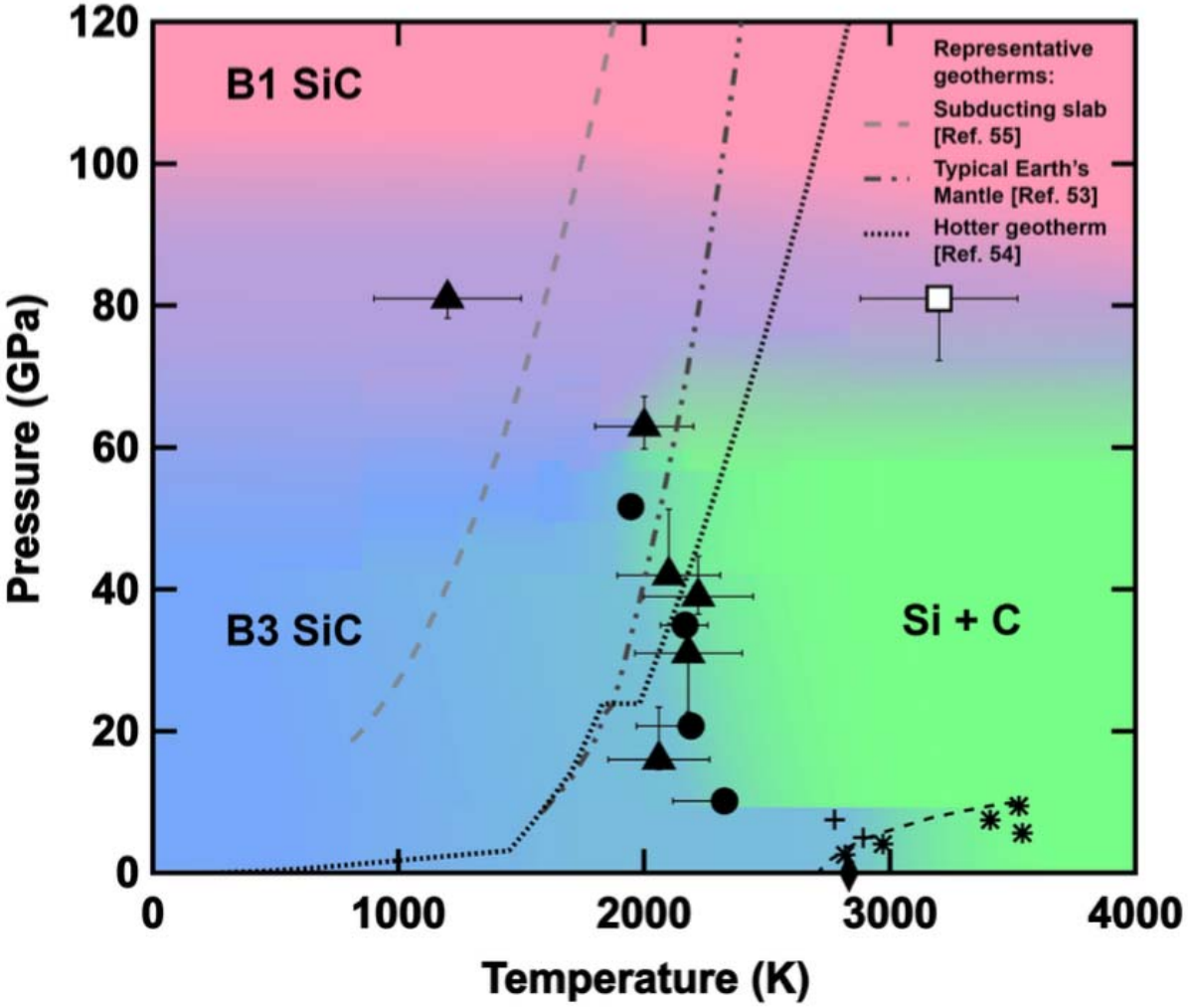

704
705
706
707
708
709
710
711
712
713
714
715
716
717
718
719

720
721 Table I. Upstream (downstream) temperatures listed for first evidence of diamond formation as
722 revealed by XRD. Uncertainties in temperatures are reported as the difference between the up
723 and downstream sides or as the difference in temperature between the last pattern without
724 diamond diffraction and the first pattern with diamond diffraction. The reported uncertainty is
725 the larger of the two (FIG. 6). *Pressure determined by Ne [20,28].

Sample Name	Pre-heat Pressure (GPa)	Pressure at diamond formation* (GPa)	Temperature at diamond formation (K)	Diamond hkl	Diamond position (d-spacing (Å))	Calculated position [a] (d-spacing (Å))
XRD_001	9.7	10.1	2327	111	2.053 (high-T)[b]	2.044
XRD_002	17.5	20.7	2160 (2223)	111 220	2.024 1.242	2.028 1.242
XRD_003	30.0	32.4	2074 (2260)	111	2.011	2.012
XRD_004	54.1	51.5	1926 (1964)	111	1.993	1.987

726 [a] Reference [63]
727 [b] At pressures of ~10 GPa the Ne 111 reflection overlaps closely with the C diamond 111
728 reflection. Because of this we use the C diamond 111 reflection collected at high-T, after Ne has
729 melted.
730
731
732 Table II. Samples heated on one side and measured by multi-wavelength imaging radiometry.
733 Uncertainties in the temperature are no more than ±8%, unless listed [24]. *Pressure determined
734 by the Raman shift of the diamond anvil [27].

Sample Name	Pre-heat Pressure* (GPa)	Post-heat Pressure* (GPa)	Insulation Media	Temperature of dark absorbing feature (K)
4CLR_001	16	24	Self-insulation	2060
4CLR_002	31	33	KCl	2180
4CLR_003	39	39	Ne	2220
4CLR_004	42	48	Self-insulation	2100
4CLR_005	63	61	Self-insulation	2000
4CLR_006	81	73 (3200 K) 79 (1200 K)	KBr	3200 (no C) 1200 (±300) (C observed)

735